Batteries & Supercaps

Research Article
doi.org/10.1002/batt.202200318

Chemistry Europe
European Chemical Societies Publishing

www.batteries-supercaps.org

Ionic Liquid-Incorporated Metal-Organic Framework with High Magnesium Ion Conductivity for Quasi-Solid-State Magnesium Batteries

Zhixuan Wei[+],*[a, b] Ruben Maile[+],[c] Luise M. Riegger,[a, b] Marcus Rohnke,[a, b] Klaus Müller-Buschbaum,*[b, c] and Jürgen Janek*[a, b]

Magnesium batteries are promising candidates for post-lithium energy storage systems due to their low cost, high volumetric energy density, and low risk of dendrite formation. This study reports a new magnesium ion conducting ionogel electrolyte based on a Metal-Organic Framework (MOF) structure (UiO-66) impregnated with an ionic liquid, magnesium bis[(trifluoromethyl)sulfonyl]imide in 1-ethyl-3-methylimidazolium bis[(trifluoromethyl)sulfonyl]imide. Comparably high conductivity of 5.7×10^{-5} S cm^{-1} can be achieved at room temperature. By employing the prepared MOF-ionogel electrolyte, a reversible quasi-solid-state magnesium battery (QSSMB) is reported. Surface analysis unveils the possible origin of the large overpotential of magnesium plating and stripping. The findings suggest that MOF-based materials are a promising class of ionogel electrolyte templates for QSSMBs. The results on the magnesium anode will be useful to define optimization strategies for magnesium metal anodes in SSMBs.

Introduction

The ever-increasing demand towards energy storage systems with both high gravimetric and volumetric energy densities calls for the exploration of new battery technologies. As an alternative for the widely studied lithium-ion batteries, magnesium-ion batteries (MIBs) have drawn considerable attention owing to the divalency and earth abundance of magnesium, giving rise to high volumetric energy density (3833 mAh cm^{-3}) as well as low manufacturing costs.[1] However, the development of MIBs is still in an initial stage due to the grand challenge of exploring suitable functional components including both electrolyte and cathode materials. This is caused by the large charge density of Mg^{2+}, which results in much stronger coulombic interaction between the charge carrier and the framework of host materials compared with the Li^+/Na^+ counterparts, leading to poor Mg mobility.[2] Furthermore, the widely used ester-based carbonate electrolytes have been reported to be not applicable in MIBs because of the ion-blocking interphase formed on the Mg metal anode during the electrochemical process.[3] Efforts have been devoted to developing other adaptive electrolytes such as Grignard reagents, non-nucleophilic salts and fluoroalkoxyborate salts, even aqueous electrolytes, etc.[4] Alternatively, solid electrolytes (SEs) are exploited, which might not only prevent the formation of the ion-blocking interphases, but also improve the safety properties by avoiding the use of flammable organic electrolytes.

The search for Mg SEs can be traced back to 1987 when Ikeda et al. reported $Mg_{0.5}Zr_2(PO_4)_3$ as a Mg-ion SE for the first time.[5] The reported conductivity of $\sim10^{-3}$ S cm^{-1} was only achieved at high temperature of 800 °C, with an activation energy of 0.82 eV. Follow-up works employed several aliovalent atoms as dopants for Zr, a real breakthrough in the conductivity has yet not been achieved.[6] In recent years, the renaissance of developing solid-state batteries[7] also, to some extent, stimulated the investigation of novel Mg-ion SEs with different crystal structures, however, successful cases are still sparse. As a class of superionic conductors for Li/Na batteries, thiophosphates have also been studied to unravel their Mg-ion conducting capability in the form of a MgS-P_2S_5-MgI_2 ceramic-glass hybrid material.[8] With the introduction of the large iodine anion, the glass framework was expanded and as a result, the ionic conductivity achieved 2.1×10^{-7} S cm^{-1} at 200 °C, but the need of elevated temperature hinders its practical application. Another class of materials, borohydrides, also emerge as promising candidates for Mg conduction due to the tunneling crystal structure that is favorable for the Mg

[a] Dr. Z. Wei,[+] L. M. Riegger, Dr. M. Rohnke, Prof. Dr. J. Janek
Institute of Physical Chemistry
Justus Liebig University Giessen
Heinrich-Buff-Ring 17, 35392 Giessen, Germany
E-mail: Zhixuan.Wei@phys.chemie.uni-giessen.de
Juergen.Janek@phys.chemie.uni-giessen.de
[b] Dr. Z. Wei,[+] L. M. Riegger, Dr. M. Rohnke, Prof. Dr. K. Müller-Buschbaum, Prof. Dr. J. Janek
Center for Materials Research (LaMa)
Justus Liebig University Giessen
Heinrich-Buff-Ring 16, 35392 Giessen, Germany
[c] R. Maile,[+] Prof. Dr. K. Müller-Buschbaum
Institute of Inorganic and Analytical Chemistry
Justus Liebig University Giessen
Heinrich-Buff-Ring 17, 35392 Giessen, Germany
E-mail: Klaus.Mueller-Buschbaum@anorg.chemie.uni-giessen.de
[+] These authors contributed equally to this work.

Supporting information for this article is available on the WWW under https://doi.org/10.1002/batt.202200318

hopping diffusion.[9] Especially, a nanocomposite of $Mg(BH_4)_2{\cdot}xNH_3$ and MgO shows a conductivity of 10^{-5} S cm^{-1} at room temperature with an activation energy of 1.12 eV where the high degree of amorphization of the composite accounts for the high Mg mobility.[10] In 2017, Ceder and his group proposed a series of ternary spinel selenides and calculated high magnesium mobility with low activation energy owing to the unfavorable tetrahedral coordination environment and related energy landscapes.[11] Experimentally, they successfully prepared $MgSc_2Se_4$ and reported a room temperature ionic conductivity of 1×10^{-4} S cm^{-1} with an activation energy of 0.38 eV, which is considered as the best Mg-ion conductor to date. However, the relatively high electronic conductivity of the selenides (10^{-8} S cm^{-1}) still needs to be taken care of towards application in all-solid-state Mg batteries. Later on, the above results on selenide spinels were also confirmed by Fichtner's group. However, decreasing the electronic conductivity still appears to be hard to achieve.[12]

Metal-organic frameworks (MOFs) with large inner surface area, flexible metal cluster/organic ligands and tunable porous structures, provide excellent templates for the design of functional materials and thus have been widely applied in the field of energy storage.[13] When used as host lattices for SEs, they can be categorized into the following three groups: MOFs 1) employed as solid fillers in composite polymer electrolytes to facilitate the dissociation of metal salts;[14] 2) as anchor in a MOF/ionic liquid composite to confine the large ions thus promoting the mobility of small ions such as Li^+;[15] and 3) as neat electrolyte via combining the open metal sites in the MOF framework with anions in the liquid electrolyte followed by drying process.[16] In 2014, Long et al. pioneered the exploration of MOF-based SEs for Mg-ion conduction.[17] They prepared a series of SEs using two MOF frameworks with different pore sizes, i.e., Mg_2(dobdc), (dobdc^{4-} = 2,5-dioxidobenzene-1,4-dicarboxylate) and Mg_2(dobpdc), (dobpdc^{4-} = 4,40-dioxidobiphenyl-3,30-dicarboxylate), to study the effect on ionic conductivity, and obtained a SE with high ionic conductivity of 0.25 mS cm^{-1} at room temperature with an activation energy of 0.13 eV. Later on, Dincă's group also reported several Mg-ion conducting SEs in Cu-azolate MOF frameworks with an upper conductivity of 0.13 mS cm^{-1}.[18] However, the use of MOF-based Mg SEs in a practical solid-state battery has not been explored. Whether they can indeed achieve reversible Mg plating/stripping and can operate with cathode active materials still remains an open question. Only very recently, Hassan et al. proposed a strategy to minimize the amount of guest solvent in MOF SEs, and meanwhile successfully assembled a symmetric Mg/Mg cell to realize reversible Mg plating/stripping.[19]

In the present paper, we report an ionogel electrolyte (IE) with high Mg-ion conductivity prepared from an ionic liquid (magnesium bis[(trifluoromethyl)sulfonyl]imide, $Mg(TFSI)_2$, dissolved in 1-ethyl-3-methylimidazolium bis[(trifluoromethyl)sulfonyl]imide, [EMIM][TFSI], hereafter denoted as MgIL); incorporated in the MOF framework ($Zr_6O_4(OH)_4(BDC)_6$, BDC = 1,4-dicarboxylate, hereafter denoted as UiO-66). The UiO-66 is constructed by linking the above $Zr_6O_4(OH)_4$ clusters with BDC linkers, giving rise to bicontinuous porous channels with tetrahedral pores (pore size of 0.75 nm) and octahedral pores (pore size of 1.2 nm),[20] respectively. In principle, both of the $[EMIM]^+$ as well as $[TFSI]^-$ could be absorbed to the well-defined porous structure of UiO-66.[21] Impressively, reversible Mg plating/stripping behavior is achieved using a MOF-IE with long-term cycling stability, which also enables the assembly of a quasi-solid-state Mg battery cell. The interface between Mg and the IE is characterized by time-of-flight secondary ion mass spectrometry method, and a F/O containing organic-inorganic composite interphase is found on the Mg foil. We believe that these results offer useful information for the further development of solid-state Mg batteries.

Results and Discussion

Structure and morphology information. The UiO-66 powder was prepared by a reported acid/base co-modulation method with slight modification.[22] The detailed procedures can be found in the experimental section. The morphology of the as-prepared UiO-66 was investigated by scanning electron microscopy (SEM). As shown in Figure 1a, the material is composed of well-dispersed nano-octahedra with an average size of ~500 nm. After addition of the MgIL, there is no significant morphological change observed, as shown in Figure 1b. Meanwhile, the composite remains as dry, free-flowing powder in appearance. Moreover, X-ray diffraction (XRD) patterns indicate that the as-prepared UiO-66 shows good crystallinity, which can be well indexed to the space group of Fm–3m with cell parameters calculated from a Pawley fit to be $a = 20.7642(5)$ Å (Figure 1c). After mixed with MgIL, no additional reflection was observed, indicating that the crystal structure of UiO-66 is well retained after incorporation of the MgIL. However, the relative intensities of (111) and (200) reflexes decrease from 2.46 to 1.32. Such change in the form factor of the MOF phase can be attributed to the change in electron density, which suggests that the MgIL has indeed been incorporated into the pore system of the framework.[23] To detect the change in the accessible porosity of the MOF framework, N_2 gas adsorption and desorption measurements were carried out. As depicted in Figure 1d, pristine UiO-66 exhibits a type I isotherm, as expected, which is characteristic of microporous materials. The Brunauer-Emmett-Teller (BET) specific surface area was calculated to be 1,242 m^2 g^{-1}. In sharp contrast, the value gets largely decreased to 21 m^2 g^{-1} after incorporating the MgIL. Meanwhile, the pore size distribution diagrams (Figure 1e) derived from the physisorption analysis via a density functional theory model suggest that the micropores (pore diameters below 2 nm) have been almost fully occupied by the ionic liquid.

To reveal the variation of the chemical environment, Fourier transform infrared spectroscopy (FTIR) measurements were carried out. As shown in Figure 1f, the bands associated with UiO-66 (678 cm^{-1}, 702 cm^{-1}, 729 cm^{-1}, 1019 cm^{-1}, 1391 cm^{-1}, 1507 cm^{-1} and 1581 cm^{-1}) are well preserved in the composite material, while several new peaks emerge in the spectrum between 1000 and 1400 cm^{-1} (marked in blue), adding

Research Article
doi.org/10.1002/batt.202200318
Chemistry Europe
European Chemical Societies Publishing

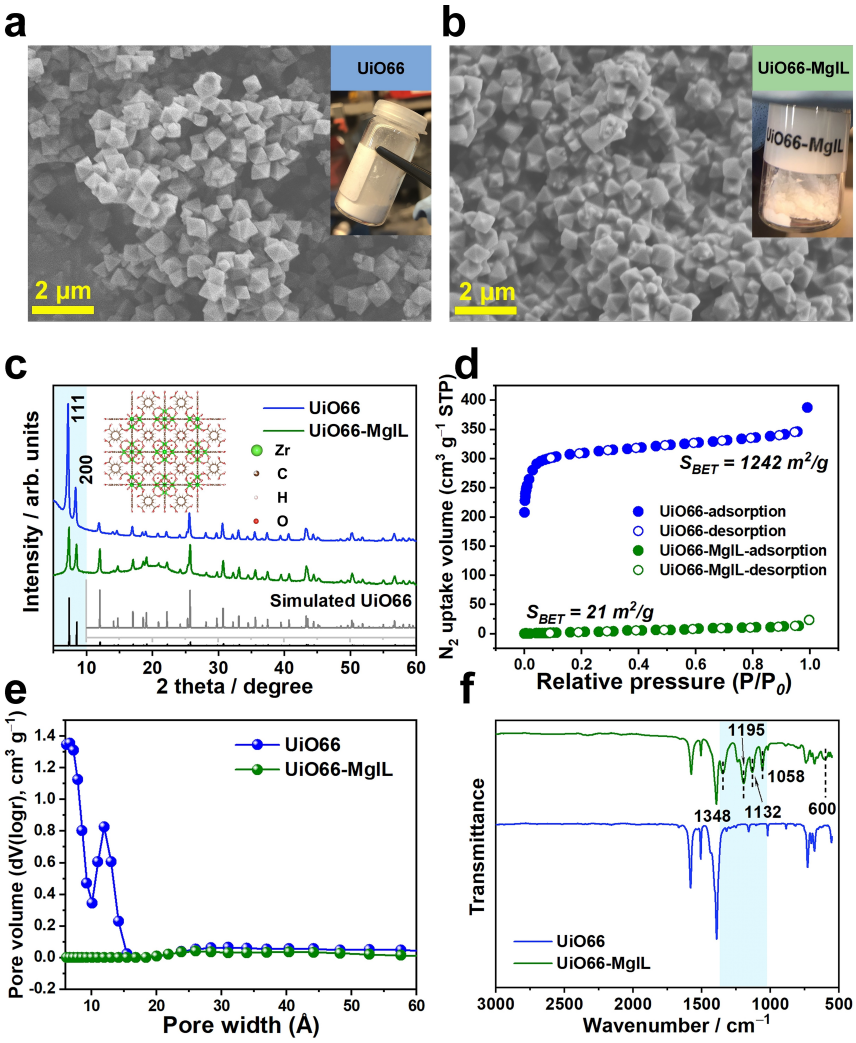

Figure 1. a) SEM image of UiO-66; b) SEM image of UiO66-MgIL electrolyte; c) XRD patterns of UiO-66 and UiO66-MgIL powder compared with simulated pattern (inset above shows the crystal structure of UiO-66 and inset below shows enlarged intensity details of the simulated reflections above 10 degrees); d) N_2 adsorption/desorption isotherms of UiO-66 and UiO66-MgIL and e) corresponding pore size distribution; f) FTIR spectra of UiO-66 and UiO66-MgIL.

evidence for the incorporation of MgIL into the hybrid material. Among them, the peaks located at 1348 cm^{-1} can be assigned to the S=O stretching;[24] the peaks at 1195 cm^{-1} and 1132 cm^{-1} can be indexed to the CF_3 stretching;[24] the peak at 1058 cm^{-1} is attributed to the asymmetric S–N–S stretching of the $TFSI^-$ anion; and the peak positioned at 600 cm^{-1} corresponds to the deformation mode of SO_2 group in $TFSI^-$ anion.[25]

The new chemical structures are also confirmed by X-ray photoelectron spectroscopy (XPS). As shown in the survey spectrum (Figure 2a), one can distinctly observe the signature peaks from the MgIL such as F-1s, Mg-2p and N-1s. In the high-resolution spectrum of the Zr-3d line (Figure 2b), the peaks caused by UiO-66 can be well recognized at binding energies of 183.3 eV and 185.8 eV for Zr-$3d_{5/2}$ and Zr-$3d_{3/2}$, respectively. Moreover, in the high-resolution spectrum of the Mg-2p line (Figure 2c), the peak located at the binding energy of 51.5 eV can be attributed to Mg^{2+} in the $Mg(TFSI)_2$ salt. Additionally, a peak from the Zr-4s line of the UiO-66 can be detected at 54.4 eV.[26] It is worth noting that the $TFSI^-$ anion is quite stable inside the mixture which is indicated by the absence of peaks from decomposition products such as MgF_2 or MgO.[27] In addition, high-resolution spectra of non-metal elements also exhibit characteristics of each component in the composite material. For the O-1s line (Figure 2d), the deconvoluted peaks can be assigned to the oxygen atoms in different functional groups in UiO-66, including the coordinated-free carboxylate group (COOH, 533.0 eV), coordinated carboxylate group (Zr–O–C, 532.3 eV) and bridging linked group (Zr–O–Zr, 530.5 eV), respectively.[28] In the high-resolution spectrum of C-1s (Figure 2e), the four fitted peaks can be indexed to C–C bonds (284.8 eV), C–O bonds (286.7 eV), O–C=O bonds (289.4 eV) from UiO-66 and the CF_3 functional group in the MgIL (293.3 eV), respectively.[29] As for the N-1s spectrum, the cationic N^+ on the $[EMIM]^+$ ring and the anionic N^- in the $[TFSI]^-$ anion can be detected at binding energies of 402.2 eV and 400.0 eV, respectively.[29b] The XPS measurements suggest that the components in the MOF-IE exhibit good compatibility with each other with no side reactions observed.

Research Article
doi.org/10.1002/batt.202200318
Chemistry Europe
European Chemical Societies Publishing

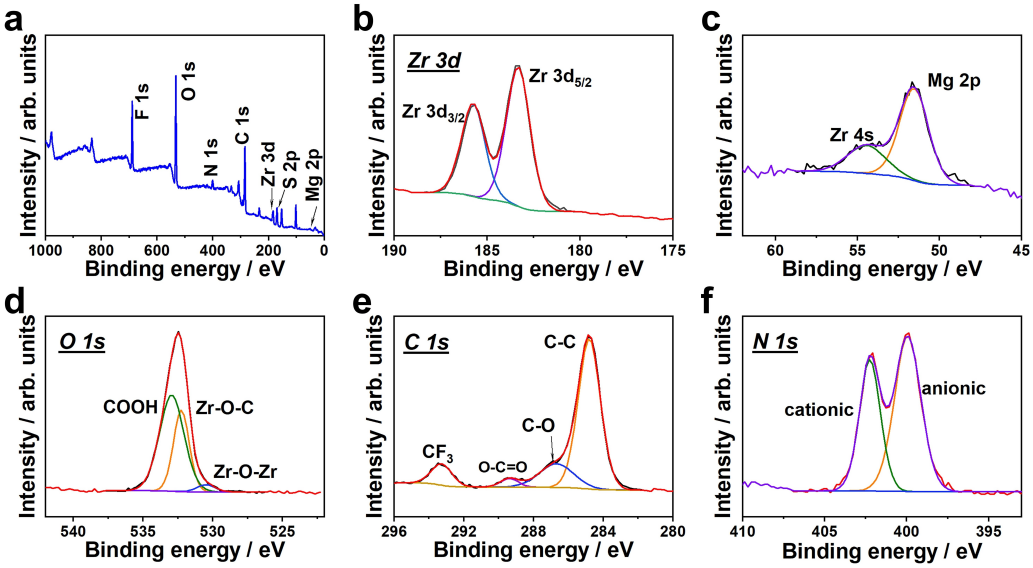

Figure 2. X-ray photoelectron spectra of the UiO66-MgIL electrolyte: a) survey spectrum; high resolution spectra of b) Zr-3d; c) Mg-2p; d) O-1s; e) C-1s and f) N-1s lines.

Conductivity measurements of UiO66-MgIL. The room temperature conductivity of the MgIL-incorporated UiO-66 was measured in symmetric cells with stainless steel as blocking electrodes. First of all, Figure S1 shows the Nyquist plots of MgIL-incorporated UiO-66 with different weight ratio. Apart from the scattered data of pure UiO-66, which is typical for a pure insulator, all of the Nyquist plots exhibit a semicircle at high frequency, corresponding to the bulk resistance (*R*) of the MOF-IE, and a tail at low frequency, which can be regarded as an imperfect capacitor (*Q*) due to the ions blocked at the electrolyte/electrode interface. According to the calculation via the above mentioned *RQ* model, the ionic conductivity increases with the increasing fraction of ionic liquid, ranging from $5.6\times10^{-6}\,S\,cm^{-1}$ to $5.8\times10^{-5}\,S\,cm^{-1}$. However, when increasing the amount of ionic liquid from the weight ratio of 1:1.25 to 1:1.5, the conductivity shows no significant change. Furthermore, as shown in Figure S2, the change of the specific surface area starts to decrease with the increasing amount of MgIL (1:1.5), suggesting that the excess amount of ionic liquid will not be fully absorbed in the pores of MOFs, which increases the risk of leakage during the battery operation. On the other hand, the excess ionic liquid also compromises the energy density of the battery, hence, the ratio of 1:1.25 was chosen for further study, and hereafter represents the reference "UiO66-MgIL". Figure S3 depicts the SEM images of the UiO66-MgIL electrolyte pellet from both top and cross-section view. The nanoparticles are densely packed with each other to form the MOF-IE pellet. Moreover, the SEM image of a cross-section and the respective elemental mappings are shown in Figure 3. The uniform distribution of the elements indicates that the MgIL is homogeneously distributed within the MOF.

Furthermore, the temperature dependence of the ionic conductivity of UiO66-MgIL was evaluated. The Nyquist plots of UiO66-MgIL at different temperatures were recorded according to the following procedure: the symmetric cell was equilibrated at 60 °C for 4 h and cooled down to 0 °C, after which the cell was heated up till 100 °C. At each temperature, the cell was thermally equilibrated for 1.5 h before the measurements

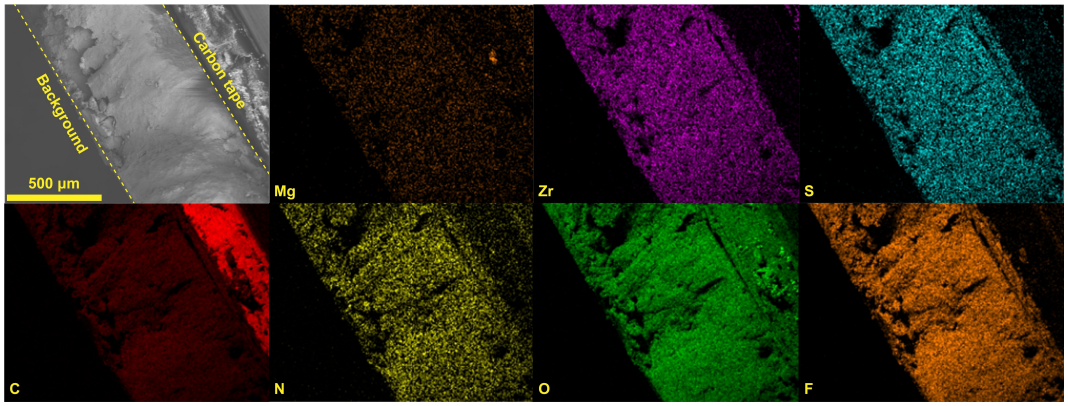

Figure 3. Cross-section SEM image of a UiO66-MgIL pellet and elemental mapping images of Mg, Zr, S, C, N, O, and F.

Research Article
doi.org/10.1002/batt.202200318
Chemistry Europe
European Chemical Societies Publishing

started. Figure 4(a and b) exhibits the results for a heating run from 0 to 100 °C, where the MOF-IE shows superior structure and thermodynamic stability, as shown in Figures S4 and S5. The ionic conductivity increases to 2.4×10^{-4} S cm^{-1} at an elevated temperature of 60 °C, which is much higher than the conductivity reported for inorganic solid state Mg-ion conductors at such mild temperatures (Figure 4c and Table S1). At a higher temperature of 100 °C, the conductivity can even increase to 1.32 mS cm^{-1}, and the chemical environment of the MOF-IE also remains unchanged, as suggested by the *ex situ* FTIR (Figure S6). As shown in Figure 4d, the activation energy of the MOF-IE can be calculated as 0.67 eV for the temperature range in which the temperature dependence of the ionic conductivity obeys the Arrhenius behavior well (between 10 °C and 60 °C).

Chemical and electrochemical stability. As a new potential Mg-ion conducting electrolyte, it is important to evaluate the chemical as well as electrochemical stability against Mg metal first. To this end, we mixed the UiO66-MgIL powder with Mg metal powder and measured the XRD pattern of the powder mixture. As shown in Figure 5a, there is no additional peak emerging except for the diffraction peaks of Mg. Moreover, we re-measured the powder XRD pattern of the mixture after storing it in the Ar-filled glovebox for two months. As can be

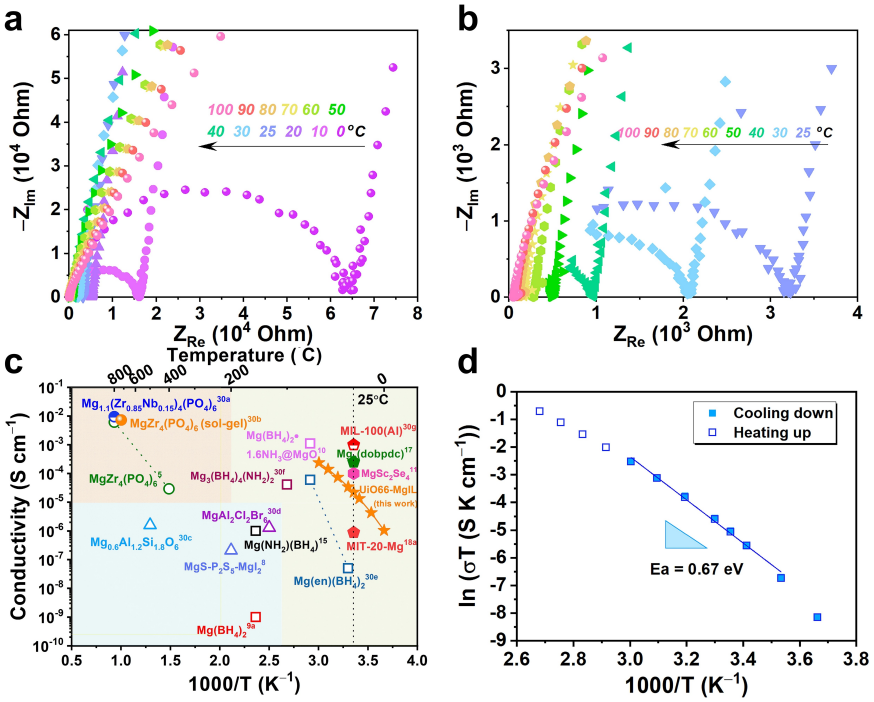

Figure 4. a) Nyquist plots of UiO66-MgIL at different temperatures ranging from 0 °C to 100 °C with b) higher resolution; c) conductivity of UiO66-MgIL and other reported solid-state Mg-ion conductors as function of temperature;[5,8,9a,10,11,17,18a,30] d) Arrhenius plot of the conductivity of UiO66-MgIL.

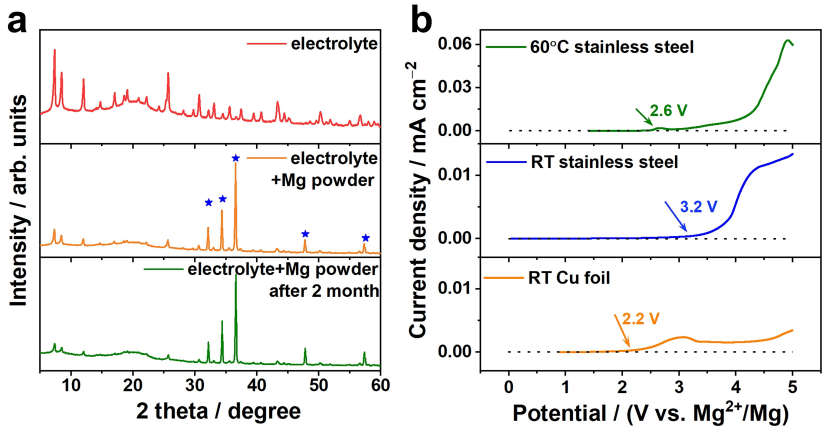

Figure 5. a) XRD pattern of the mixture UiO66-MgIL electrolyte powder with Mg powder compared with the pristine powder (blue asterisks indicate the reflections from Mg); b) LSV curves of Mg | UiO66-MgIL | Cu/stainless steel recorded at scan rate of 0.1 mV s^{-1} tested at room temperature and 60 °C, respectively.

Research Article
doi.org/10.1002/batt.202200318
Chemistry Europe
European Chemical Societies Publishing

seen in the diffraction pattern, the peak positions are well retained, as well as the relative intensities between UiO66-MgIL and Mg reflections. The above results indicate superior chemical stability of UiO66-MgIL against Mg. Furthermore, the oxidation onset potential of the MOF-IE was measured via linear sweep voltammetry (LSV) from open circuit voltage (OCV) to 5 V (vs. Mg^{2+}/Mg) with a scan rate of 0.1 mV s^{-1} in asymmetric cells, where Mg foils were used as counter and reference electrode; different current collectors were used as working electrode. As shown in Figure 5b, at room temperature, the oxidation current of the electrolyte starts to grow from 2.2 V for the Cu electrode. In contrast, the cathodic limit can be widened to 3.2 V when using stainless steel as current collector, which is the highest value for the state-of-the-art Mg-ion conductors for solid-state Mg batteries (Table S1). At an elevated temperature of 60 °C, the current response of the Mg | UiO66-MgIL | stainless steel cell is stronger and the onset potential decreased to 2.6 V, where a small hump appears. Even so, the electrochemical stability of the electrolyte till 2.6 V is suitable for most of the transition metal chalcogenide cathode materials for Mg-ion batteries that have been reported.[31]

Mg plating/stripping behavior. To validate the applicability of the UiO66-MgIL IE in a quasi-solid-state cell, initially, symmetric cells with Mg foil electrodes were assembled and tested at 60 °C. First of all, to evaluate the critical current density (CCD), the potential profile at different applied currents from 1 μA to 50 μA was recorded. As shown in Figure S7, a short circuit of the cell did not occur, but the overpotential of Mg plating/stripping already reaches 4 V vs. Mg^{2+}/Mg when the current is increased to 50 μA. Afterwards, the overpotential did not return to a smaller value even when the current decreases back to 10 μA. Compared with lithium or sodium counterparts, such a pronounced voltage hysteresis may be attributed to the large energy barrier for the movement of double-charged Mg^{2+} ions. We notice that, beyond 20 μA, a steady-state voltage after Mg nucleation cannot be achieved in the potential profile, and the overpotential already reaches the oxidation onset potential of the electrolyte, hence, the CCD is determined to be 31.4 μA cm^{-2} ($I = 20$ μA). Accordingly, the long-term cycling performance was investigated at different current densities. At 1.57 μA cm^{-2} (Figure 6a), the symmetric cell exhibits an overpotential reaching around 0.45 V in the first several cycles (closer look in Figure S8). The overpotential is much larger than the estimated IR drop of 0.33 mV across the MOF-IE itself determined from the ionic conductivity (2.4×10^{-4} S cm^{-1} at 60 °C), suggestive of an interface-dominating resistance inside the symmetrical cell. As shown in Figures S9 and S10, although using elevated temperature can significantly facilitate the Mg transfer at the interface by improving the solid-solid contact, the resistance still reaches 277,000 Ohm at 60 °C, giving rise to an overpotential of 0.28 V, which is consistent with the initial overpotential value in *E-t* profile. Subsequently, the overpotential increases to 0.45 V followed by decreasing and then gets stabilized at nearly 0.25 V, which could be attributed to the formation of a stable electrolyte/electrode interface. It is worth highlighting that the XRD pattern of the cycled UiO66-MgIL electrolyte pellet shows no additional peaks compared with the pristine electrolyte powder (Figure S11), which again confirms its good chemical stability against Mg metal. At a higher current density (3.14 μA cm^{-2}), the overpotential of the symmetric battery also shows an increasing trend at the beginning and then stabilized at 0.8 V (Figure 6b, closer look in Figure S12). After the activation process, the battery was cycled for 200 h, demonstrating superior electrochemical stability. Moreover, compared with the pristine Mg foil (Figure 6c), the smooth surface of the Mg foil after the long-cycling test was well retained without dendrite formation, as shown in the *ex-situ* SEM image (Figure 6d). If we prolong the reaction time of each step (charge and discharge) from 30 min to 600 min, the symmetric cell can still work for 10 cycles, as shown in Figure S13a. Nevertheless, the cell fails afterwards due to the pronounced surface reaction, as indicated by the rougher interface on top of Mg foil shown in the SEM images (Figure S13b and c). Hence, an appropriate surface modification method still needs to be found to protect the metal anode, and further enhance the kinetic properties on the other hand.

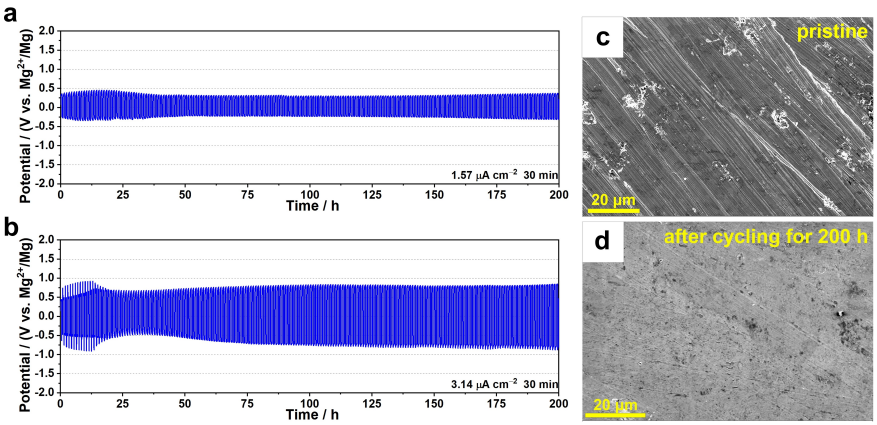

Figure 6. Long-term cycling performance during Mg plating/stripping at current densities of a) 1.57 μA cm^{-2}; b) 3.14 μA cm^{-2} for 30 min charge and 30 min discharge in each cycle; SEM image of the c) pristine Mg foil and d) Mg foil after cycling test at 3.14 μA cm^{-2}. All the cells were measured at 60 °C.

Research Article
doi.org/10.1002/batt.202200318
Chemistry Europe
European Chemical Societies Publishing

Surface analysis. To unravel the reason for the high overpotential, we carried out time-of-flight secondary ion mass spectrometry (ToF-SIMS) measurements to elucidate the surface composition of the cycled Mg foils. Figure 7 depicts the mass spectra recorded in the negative ion mode as well as the depth profiles revealing the evolution of several species of interest on the surface. First of all, as shown in Figures 7d and S14, the absence of Zr-containing fragments (such as ZrO^-) on the Mg foil surface eliminates the possible presence of MOF-IE residuals on the Mg anode area, because all elements are homogeneously distributed throughout the IE pellet (Figure 3). Hence, the recorded profiles are indeed offering information on the interlayer formed between electrolyte and Mg foil. Especially, the signals of F^- and CN^- fragments are much more pronounced compared with the pristine Mg foil (Figure 7a), indicative of the major contribution of the $[TFSI]^-$ anions degradation to the interlayer components. Apart from the inorganic fragments (MgF^-, Figure 7i), organic species containing F also contribute to the interlayer, whose possible components are marked in Figure 7c. Moreover, as suggested in Figure 7e, h, i and j, when the F-containing species gradually diminished to the background level after the sputtered Argon-ion dose reaches 2×10^{17} ions cm^{-2}, the numbers of counts of O-containing fragments are still quite stable, suggesting a quite thick interlayer containing oxygen. The phenomenon can be attributed to the strong affinity of Mg with oxygen, which suggests the formation of MgO. The surface element mapping of pristine Mg foil can also serve as further evidence. As shown in Figure S15, even though the Mg foil is polished until the shiny metal part is uncovered, oxygen is hard to be fully eliminated. Since these components of the interlayer, such as MgO and MgF_2 show high migration barriers for Mg^{2+} transport (1.85 eV and 1.12 eV, respectively),[32] the Mg plating/stripping exhibits quite large overpotential. Surface modification targeting the formation of more Mg conductive phases or interphases (such as Mg halides), can be the up-coming strategy towards a smaller overpotential as well as a higher CCD in Mg solid-state batteries.

Full cell performance. Encouraged by the long-term Mg stripping/plating cycling stability, a quasi-solid-state Mg battery (QSSMB) has been successfully assembled using an organic molecule, perylenetetracarboxylic dianhydride (PTCDA) as cathode,[33] a UiO66-MgIL pellet as electrolyte and Mg foil as anode. Compared with inorganic cathode materials, the more flexible structure as well as the more accessible redox sites of organic molecules could compensate the diffusion penalty of the double-charged Mg ions to a large extent. The structural information of PTCDA can be found in Figure 8a. PTCDA crystallizes in a monoclinic structure, where the molecules are packed into stacking structure via weak Van der Waals interaction. Galvanostatic charge and discharge profiles of the QSSMB were recorded in the voltage range between 0.3 and 2.5 V (vs. Mg^{2+}/Mg). As shown in Figure 8b, the profiles exhibit a long plateau in the discharge curves and two sequential plateaus in the charge process located at 1.8 V and 2.2 V, respectively, representing the enolization process of the C=O in the PTCDA molecule after Mg insertion.[34] The redox reaction demonstrates good reversibility for the initial cycle, with a reversible capacity reaching 27.7 mAh g^{-1}. However, the capacity shows decay in the following cycles. Meanwhile, a large voltage hysteresis of the redox reaction can be observed as expected due to the large interfacial resistance at the anode

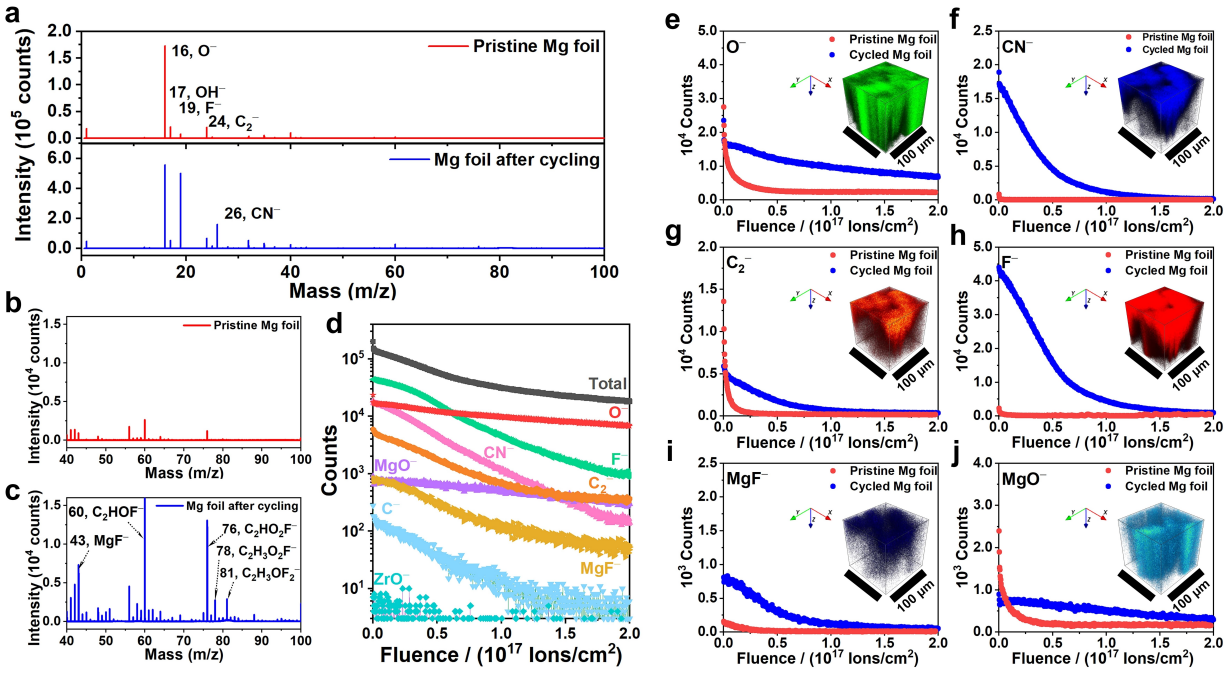

Figure 7. ToF-SIMS analysis of a Mg foil after symmetric cycling test. Analysis was carried out in negative ion mode with Bi_3^{++} primary ions. a–c) Selected ion spectra of cycled Mg foil compared with pristine Mg foil; d) depth profile of the cycled Mg foil applying Ar cluster ions and e–j) the corresponding high-resolution profiles of the species of interest compared with the pristine Mg foil (insets show 3D reconstruction of sputtered volume of the cycled Mg foil).

Research Article
doi.org/10.1002/batt.202200318
Chemistry Europe
European Chemical Societies Publishing

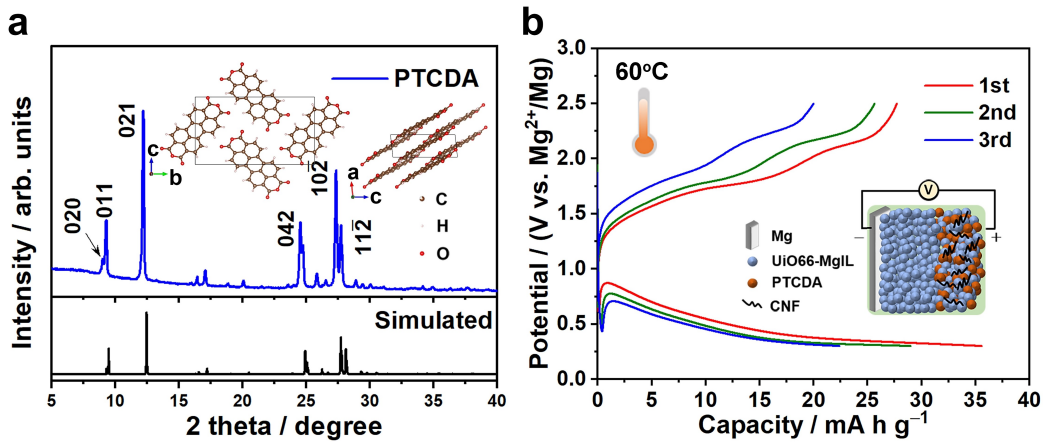

Figure 8. a) XRD pattern of PTCDA powder in comparison with the simulated pattern (inset shows the crystal structure of PTCDA); b) galvanostatic charge and discharge profiles of PTCDA at a current rate of 1 mA g^{-1} (inset shows the QSSMB cell configuration).

side. Even so, the feasibility of the proof-of-concept QSSMB can be considered as a good starting point, whose reversible capacity and rate capability can be further enhanced once the Mg anode is optimized by suitable surface engineering, as mentioned above.

Conclusion

In sum, we report a new MOF-ionogel electrolyte with high room-temperature ionic conductivity of 5.7×10^{-5} S cm^{-1} as well as elevated conductivity of 2.4×10^{-4} S cm^{-1} at 60 °C. By virtue of the good Mg mobility, reversible and stable Mg plating/stripping was realized, which can be cycled for 200 times without dendrite formation, however, at low current density and correspondingly low cycled charge. ToF-SIMS analysis shows that an oxygen- and fluorine-rich organic/inorganic composite interphase forms on the surface of Mg foil during cycling, and the high Mg migration barrier across this interphase may be the origin of the large Mg redox overpotential during the battery operation. Moreover, the electrolyte material employed in this paper shows a breakthrough by demonstrating a proof-of-concept QSSMB with PTCDA cathode that can work at a mild temperature (60 °C). We hope that the reported work could inspire the functional design of QSSMBs/SSMBs based on MOF-structured ionogel electrolytes.

Experimental Section

Materials. $ZrCl_4$ (abcr, 99.95 %), 1,4-dicarboxylate (BDC, abcr, 98 %), Magnesium bis (trifluoromethanesulfonyl) imide [$Mg(TFSI)_2$, TCI, > 97 %], 1-ethyl-3-methylimidazolium bis (trifluoromethanesulfonyl) imide ([EMIM][TFSI], TCI, > 98 %), Mg foil (Sigma-Aldrich 99.9 %) and PTCDA (Sigma-Aldrich, 97 %).

Synthesis of UiO-66. The UiO-66 was synthesized according to a previous report with slight modification.[22] Firstly, 560 mg dry $ZrCl_4$ (2.4 mmol) powder were dissolved in 30 mL N,N-dimethylformamide (DMF). Subsequently, 430 mg BDC (2.4 mmol) were dissolved in a mixture of 280 mL DMF, 40 mL acetic acid and 0.15 mL triethylamine (TEA) in another flask and heated to 120 °C. After dissolution of BDC, the $ZrCl_4$ solution was added and the mixed solution reacted at 120 °C for 6 h under reflux. Afterwards, the solution was cooled down to room temperature, and the final product was collected by centrifugation at 4000 rpm for 5 min followed by washing several times with DMF. The obtained white powder was activated at 150 °C for 24 h under vacuum before use.

Preparation of ionogel electrolyte. $Mg(TFSI)_2$ powder was dried at 150 °C for 24 h under vacuum before use, while the ionic liquid, [EMIM][TFSI], was directly used as received. The whole procedure of the preparation of electrolyte was carried out in an Argon-filled glove box. Firstly, the $Mg(TFSI)_2$ powder was dissolved in [EMIM][TFSI] with a concentration of 1 M at 100 °C. After the powder was dissolved, the transparent solution was cooled down to room temperature before use. Afterwards, the ionogel electrolyte powder was obtained by thoroughly mixing the UiO-66 powder and 1 M $Mg(TFSI)_2$-[EMIM][TFSI] ionic liquid with different weight ratio via hand-milling in an agate mortar for 15 min and aged at 60 °C for 3 hours.

Material characterization. The *powder X-ray diffraction* patterns were collected on an Empyrean powder diffractometer (Malvern Panalytical Ltd) using Cu K_α radiation (λ_1 = 1.5405980 Å; λ_2 = 1.5444260 Å) in reflection geometry. IE-containing samples were sealed with Kapton film inside the glovebox to avoid air and humidity. Data were recorded in the 2θ range from 5° to 60° with a step size of 0.026°. Standard cif. files for generating simulated XRD pattern were obtained from crystallography open database (No. 4512072 for UiO-66 and No. 8100631 for PTCDA). Cell parameters of UiO-66 were obtained by Pawley fit on Topas refinement software. *For In situ heating XRD*, Reactor Chamber XRK 900 (Anton Paar GmbH) was used. The MOF-IE powder was measured from 25 °C to 150 °C with temperature interval of 25 °C, under He atmosphere. Before each measurement, the material was kept at the corresponding temperature for 30 min. *SEM images* were obtained with a Zeiss Merlin instrument at an acceleration voltage of 4 kV and 3 kV for Mg foil and UiO-66 containing material, respectively. For *EDX mapping*, an X-MAX 50 detector (Oxford Instruments, U.K.) was used at an acceleration voltage of 4 kV and 5 kV for the Mg foil and the IE pellet, respectively. For the cross-section measurements, an IE pellet was manually broken in halves and then attached to the sample holder. To avoid air contamination, the samples were transferred from the Ar-filled glovebox to SEM chamber via a Leica transfer module (EM VCT 500). *FTIR* was conducted on a NICOLET iS 10 FTIR spectrometer (Thermo Fisher

Scientific), which is positioned in the glovebox. *N_2 adsorption/desorption isotherms* were recorded via an Autosorb-1 of quantachrome instrument. Pore size distribution was obtained by density functional method which was included in the program ASiQwin. The model used is: N_2 at 77 K on silica, cylinder pore, NLDFT equilibrium model. *XPS measurements* were carried out on a PHI 5000 VersaProbe II Scanning ESCA Microprobe (Physical Electronics) with a monochromatized Al K_α source (1486.6 eV). The beam had a diameter of 200 μm and a power of 50 W. For the detailed spectra, a step size of 0.2 eV, step time of 50 ms and analyzer pass energy of 46.95 eV were used. The sample surface was charge neutralized with slow electrons and argon-ions. The XPS data was analyzed using the CasaXPS software, where Shirley-type background correction was applied. Before fitting, all the peaks were calibrated relative to the signal of adventitious carbon (284.8 eV). *Thermogravimetric analysis* (TGA, NETZSCH STA-409-PC) was recorded from room temperature to 800 °C in Ar with a ramping rate of 5 °C min^{-1}. The argon flow was 50 mL min^{-1}. *ToF-SIMS characterizations* were conducted via a Hybrid SIMS M6 system (IONTOF GmbH, Germany). The analysis was carried out with 60 keV Bi_3^{++} ions with the 1100 aperture resulting in a primary ion current of 0.7 pA @ 110 μs cycle times. Therefore, the primary ion gun was operated in spectrometry (high-current-bunched mode). All spectra were recorded with the analyzer in all-purpose mode resulting in a mass resolution (FWHM) of $m/\Delta m$ better than 8,000 for CN^- (26.01). For charge compensation, low energetic electron flooding was carried out. For depth profiling, 10 keV Ar_{1232}^+ cluster ions (cluster size at maximum of distribution) were applied ($I = 10.46$ nA). The analysis area was set to $100 \times 100\ \mu m^2$ centered within a $200 \times 200\ \mu m^2$ sputter area. The measurements were carried out in negative polarity. The samples were also transferred to the chamber via Leica transfer module (EM VCT 500) to avoid air exposure. After the profiles were collected, data analysis was performed with the SurfaceLab 7.2 software (IONTOF GmbH, Germany).

Cell assembly and electrochemical measurements. All of the electrochemical cells used in this work were assembled in a home-designed battery cell casing as described in our previous report,[35] and all of the electrochemical tests were performed with a VMP300 electrochemical workstation from Bio-Logic Science Instruments SAS. For ionic conductivity measurements, MOF-IE powder was filled in the PEEK housing with a diameter of 10 mm. Stainless steel stamps serve as blocking electrodes. The symmetric cell was pressed at 3 tons for 3 min where MOF-IE pellets form inside the PEEK housing; aged in an oven at 60 °C for 4 h, and then cooled down to room temperature before the measurements. The electrochemical impedance measurements were carried out in the frequency range from 3 MHz–100 mHz by applying a 10 mV amplitude voltage. Ionic conductivities were calculated based on the following equation:

$$\sigma = \frac{1}{R} \cdot \frac{l}{A}$$

where R is the bulk resistance obtained from intercept of the semicircle in Nyquist plots, while l and A represent the thickness and area of the IE pellet, respectively. For temperature dependence measurements, a climate chamber (Weisstechnik) was used. Impedance spectra were recorded between 0 °C and 100 °C after kept at the certain temperature for 1.5 h. The activation energy (E_a) was determined according to the Arrhenius equation:

$$\sigma = \frac{\sigma_0}{T} \exp\left(-\frac{E_a}{k_B T}\right)$$

with σ_0 being the conductivity prefactor. For LSV measurements, a MOF-IE pellet was pressed (same as the procedures making symmetric cells). Then, the polished Mg foil ($\phi = 9$ mm) was put on one side of the IE pellet. In the case of Mg|UiO66-MgIL|Cu cells, Cu foil ($\phi = 9$ mm) was put on the other side of electrolyte pellet. For electrochemical measurements of Mg|UiO66-MgIL|Mg cells, polished Mg foils with diameter of 9 mm were placed on both sides of the IE pellet. For the fitting of impedance spectrum of the symmetric cell, RelaxIS software package (rhd instruments, Version 3) was used. For electrochemical measurements of Mg|UiO66-MgIL|PTCDA full cells, PTCDA powder was used as received. Cathode composites were first prepared by mixing PTCDA with UiO66-MgIL and carbon nanofibers with a weight ratio of 6:5:1. Then, after preparing the IE pellet, the cathode composite powder was spread onto one side of the pellet, while polished Mg foil ($\phi = 9$ mm) was put on the other side of the pellet. Finally, the cell was again pressed at 3 tons for 1 min and activated via a complete charge/discharge cycle. During the electrochemical measurements, a constant pressure was applied on the cells by using the screw of aluminum framework with 10 N m torque.

Acknowledgements

This work was funded by the German Research Foundation (DFG) under Project ID 390874152 (POLiS Cluster of Excellence). Financial support by BMBF (Federal Ministry of Education and Research, Germany) within the FESTBATT Cluster of Competence (project 03XP0177A) is also acknowledged. The authors would like to thank Felix Hartmann for the valuable discussion on XRD results. We also thank Alexander Sedykh for the TGA measurement. Open Access funding enabled and organized by Projekt DEAL.

Conflict of Interest

The authors declare no conflict of interest.

Data Availability Statement

The data that support the findings of this study are available from the corresponding author upon reasonable request.

Keywords: interface · ionic liquids · ionogel electrolyte · magnesium battery · metal-organic frameworks

[1] a) D. Aurbach, Z. Lu, A. Schechter, Y. Gofer, H. Gizbar, R. Turgeman, Y. Cohen, M. Moshkovich, E. Levi, *Nature* **2000**, *407*, 724–727; b) Y. Liang, H. Dong, D. Aurbach, Y. Yao, *Nat. Energy* **2020**, *5*, 646–656.
[2] a) M. Dillenz, M. Sotoudeh, C. Glaser, J. Janek, A. Groß, H. Euchner, *Batteries & Supercaps* **2022**, *5*, e202200164; b) L. Blanc, C. J. Bartel, H. Kim, Y. Tian, H. Kim, A. Miura, G. Ceder, L. F. Nazar, *ACS Materials Lett.* **2021**, *3*, 1213–1220.
[3] D. Aurbach, Y. Gofer, A. Schechter, O. Chusid, H. Gizbar, Y. Cohen, M. Moshkovich, R. Turgeman, *J. Power Sources* **2001**, *97*, 269–273.
[4] a) S. Hou, X. Ji, K. Gaskell, P.-f. Wang, L. Wang, J. Xu, R. Sun, O. Borodin, C. Wang, *Science* **2021**, *374*, 172–178; b) R. Dominko, J. Bitenc, R. Berthelot, M. Gauthier, G. Pagot, V. D. Noto, *J. Power Sources* **2020**, *478*, 229027; c) L. Chen, J. L. Bao, X. Dong, D. G. Truhlar, Y. Wang, C. Wang, Y. Xia, *ACS Energy Lett.* **2017**, *2*, 1115–1121.

[5] S. Ikeda, M. Takahashi, J. Ishikawa, K. Ito, *Solid State Ionics* **1987**, *23*, 125–129.
[6] a) N. Imanaka, Y. Okazaki, G. Adachiz, *Electrochem. Solid-State Lett.* **2000**, *3*, 327–329; b) B. Liang, V. Keshishian, S. Liu, E. Yi, D. Jia, Y. Zhou, J. Kieffer, B. Ye, R. M. Laine, *Electrochim. Acta* **2018**, *272*, 144–153.
[7] a) R. Chen, Q. Li, X. Yu, L. Chen, H. Li, *Chem. Rev.* **2020**, *120*, 6820–6877; b) S. Randau, D. A. Weber, O. Kötz, R. Koerver, P. Braun, A. Weber, E. Ivers-Tiffée, T. Adermann, J. Kulisch, W. G. Zeier, F. H. Richter, J. Janek, *Nat. Energy* **2020**, *5*, 259–270.
[8] T. Yamanaka, A. Hayashi, A. Yamauchi, M. Tatsumisago, *Solid State Ionics* **2014**, *262*, 601–603.
[9] a) S. Higashi, K. Miwa, M. Aoki, K. Takechi, *Chem. Commun.* **2013**, *50*, 1320–1322; b) J. Cuan, Y. Zhou, T. Zhou, S. Ling, K. Rui, Z. Guo, H. Liu, X. Yu, *Adv. Mater.* **2019**, *31*, 1803533.
[10] Y. Yan, J. B. Grinderslev, M. Jørgensen, L. N. Skov, J. Skibsted, T. R. Jensen, *ACS Appl. Energ. Mater.* **2020**, *3*, 9264–9270.
[11] P. Canepa, S.-H. Bo, G. S. Gautam, B. Key, W. D. Richards, T. Shi, Y. Tian, Y. Wang, J. Li, G. Ceder, *Nat. Commun.* **2017**, *8*, 1759.
[12] L.-P. Wang, Z. Zhao-Karger, F. Klein, J. Chable, T. Braun, A. R. Scher, C.-R. Wang, Y.-G. Guo, M. Fichtner, *ChemSusChem* **2019**, *12*, 2286–2293.
[13] Z. Ye, Y. Jiang, L. Li, F. Wu, R. Chen, *Nano-Micro Lett.* **2021**, *13*, 203.
[14] H. Huo, B. Wu, T. Zhang, X. Zheng, L. Ge, T. Xu, X. Guo, X. Sun, *Energy Storage Mater.* **2019**, *18*, 59–67.
[15] a) J. Wu, X. Guo, *Small* **2019**, *15*, 1804413; b) X. Yu, N. S. Grundish, J. B. Goodenough, A. Manthiram, *ACS Appl. Mater. Interfaces* **2021**, *13*, 24662–24669.
[16] a) L. Shen, H. B. Wu, F. Liu, J. L. Brosmer, G. Shen, X. Wang, J. I. Zink, Q. Xiao, M. Cai, G. Wang, Y. Lu, B. Dunn, *Adv. Mater.* **2018**, *30*, 1707476; b) R. Zettl, S. Lunghammer, B. Gadermaier, A. Boulaoued, P. Johansson, H. M. R. Wilkening, I. Hanzu, *Adv. Energy Mater.* **2021**, *11*, 2003542.
[17] M. L. Aubrey, R. Ameloot, B. M. Wiers, J. R. Long, *Energy Environ. Sci.* **2014**, *7*, 667–671.
[18] a) S. S. Park, Y. Tulchinsky, M. Dincă, *J. Am. Chem. Soc.* **2017**, *139*, 13260–13263; b) E. M. Miner, S. S. Park, M. Dincă, *J. Am. Chem. Soc.* **2019**, *141*, 4422–4427.
[19] H. K. Hassan, A. Farkas, A. Varzi, T. Jacob, *Batteries & Supercaps* **2022**, doi: 10.1002/batt.202200260.
[20] F. P. Kinik, A. Uzun, S. Keskin, *ChemSusChem* **2017**, *10*, 2842–2863.
[21] L. Sun, K. Zhuo, Y. Chen, Q. Du, S. Zhang, J. Wang, *Adv. Funct. Mater.* **2022**, 2203611.
[22] Y. Zhao, Q. Zhang, Y. Li, R. Zhang, G. Lu, *ACS Appl. Mater. Interfaces* **2017**, *9*, 15079–15085.
[23] X. Liu, M. Kozlowska, T. Okkali, D. Wagner, T. Higashino, G. Brenner-Weiß, S. M. Marschner, Z. Fu, Q. Zhang, H. Imahori, S. Bräse, W. Wenzel, C. Wöll, L. Heinke, *Angew. Chem. Int. Ed.* **2019**, *58*, 9590–9595; *Angew. Chem.* **2019**, *131*, 9691–9696.
[24] D. Hambali, Z. Osman, L. Othman, K. B. M. Isa, N. Harudin, *J. Polym. Res.* **2020**, *27*, 159.
[25] Shalu, V. K. Singh, R. K. Singh, *J. Mater. Chem. C* **2015**, *3*, 7305–7318.
[26] J. Chastain, R. C. King Jr, in *Handbook of X-ray photoelectron spectroscopy*. Perkin-Elmer, USA, **1992**, 261.
[27] a) M. S. Ding, T. Diemant, R. J. Behm, S. Passerini, G. A. Giffin, *J. Electrochem. Soc.* **2018**, *165*, A1983–A1990; b) Y. He, Q. Li, L. Yang, C. Yang, D. Xu, *Angew. Chem. Int. Ed.* **2019**, *58*, 7615–7619; *Angew. Chem.* **2019**, *131*, 7697–7701.
[28] Y. Wang, L. Li, P. Dai, L. Yan, L. Cao, X. Gu, X. Zhao, *J. Mater. Chem. A* **2017**, *5*, 22372–22379.
[29] a) C. Chen, D. Chen, S. Xie, H. Quan, X. Luo, L Guo, *ACS Appl. Mater. Interfaces* **2017**, *9*, 41043–41054; b) P. Sedlak, D. Sobola, A. Gajdos, R. Dallaev, A. Nebojsa, P. Kubersky, *Polymer* **2021**, *13*, 2678.
[30] a) J. Kawamura, K. Morota, N. Kuwata, Y. Nakamura, H. Maekawa, T. Hattori, N. Imanaka, Y. Okazaki, G.-y. Adachi, *Solid State Commun.* **2001**, *120*, 295–298; b) M. Adamu, G. M. Kale, *J. Phys. Chem. C* **2016**, *120*, 17909–17915; c) H. Takeda, K. Nakano, N. Tanibata, M. Nakayama, *Sci. Technol. Adv. Mater.* **2020**, *21*, 131–138; d) Y. Tomita, R. Saito, M. Morishita, Y. Yamane, Y. Kohno, *Solid State Ionics* **2021**, *361*, 115566; e) E. Roedern, R.-S. Kühnel, A. Remhof, C. Battaglia, *Sci. Rep.* **2017**, *7*, 46189; f) R. L. Ruyet, B. Fleutot, R. Berthelot, Y. Benabed, G. Hautier, Y. Filinchuk, R. Janot, *ACS Appl. Energ. Mater.* **2020**, *3*, 6093–6097; g) S. Ma, L. Shen, Q. Liu, W. Shi, C. Zhang, F. Liu, J. A. Baucom, D. Zhang, H. Yue, H. B. Wu, Y. Lu, *ACS Appl. Mater. Interfaces* **2020**, *12*, 43824–43832.
[31] C. Pei, F. Xiong, Y. Yin, Z. Liu, H. Tang, R. Sun, Q. An, L. Mai, *Small* **2021**, *17*, 2004108.
[32] T. Chen, G. S. Gautam, P. Canepa, *Chem. Mater.* **2019**, *31*, 8087–8099.
[33] a) W. Luo, M. Allen, V. Raju, X. Ji, *Adv. Energy Mater.* **2014**, *4*, 1400554; b) Y. Chen, W. Luo, M. Carter, L. Zhou, J. Dai, K. Fu, S. Lacey, T. Li, J. Wan, X. Han, Y. Bao, L. Hu, *Nano Energy* **2015**, *18*, 205–211.
[34] I. A. Rodríguez-Pérez, Y. Yuan, C. Bommier, X. Wang, L. Ma, D. P. Leonard, M. M. Lerner, R. G. Carter, T. Wu, P. A. Greaney, J. Lu, X. Ji, *J. Am. Chem. Soc.* **2017**, *139*, 13031–13037.
[35] W. Zhang, D. A. Weber, H. Weigand, T. Arlt, I. Manke, D. Schröder, R. Koerver, T. Leichtweiss, P. Hartmann, W. G. Zeier, J. Janek, *ACS Appl. Mater. Interfaces* **2017**, *9*, 17835–17845.

Manuscript received: July 13, 2022
Revised manuscript received: September 27, 2022
Accepted manuscript online: September 28, 2022
Version of record online: October 26, 2022